RSC Advances

PAPER

View Article Online
View Journal | View Issue

Published on 10 December 2014. Downloaded by Tamkang University Libraries on 19/01/2015 03:58:08.

Cite this: *RSC Adv.*, 2015, **5**, 7897

Thermally evaporable 5,10-dihydroindeno[2,1-*a*]indenes form efficient interfacial layers in organic solar cells†

Yi Wei,*[a] Pei-Jun Liu,[a] Ren-Hao Lee[b] and Chih-Ping Chen*[bc]

Received 3rd October 2014
Accepted 10th December 2014

DOI: 10.1039/c4ra11696h

www.rsc.org/advances

In this study, we synthesized several bis(diarylamino)dihydroindenoindene derivatives for use as small-molecule hole transporting materials (HTMs) in organic photovoltaics. Because of their photophysical, electrochemical, and morphological properties, as well as their surface energies and device structures, these barely soluble HTMs prohibited interfacial mixing during the subsequent deposition through spin-coating of the active layer. An optimized device having the structure indium tin oxide/HTM/P3HT:PCBM/Ca/Al operated with a fill factor of 67.8%.

Introduction

The energy generated in our modern societies is derived mainly from petroleum and nuclear power. Unfortunately, the natural resources required for these power sources are not sustainable. In addition, the combustion of gasoline also produces large quantities of greenhouse gases, which may have catastrophic consequences as a result of global warming. Accordingly, there is a major quest underway to discover sources of renewable energy.

It has been estimated that the world's energy consumption will reach 28 TW in 2050.[1,2] Solar energy is a promising source of energy because sunlight strikes he Earth's surface with 1.7×10^5 TW of light and heat every year. Based on the Frank–Condon principle, appropriately designed molecules undergo electronic transitions when exposed to sunlight.[3,4] This property can be applied for the development of photovoltaic cells. In particular, organic photovoltaics (OPVs) have the merits of low cost, stability, simple fabrication, and flexibility.[5–13] The performance of an OPV cell is enhanced significantly when using a bulk heterojunction (BHJ) structure, which allows efficient charge separation,[14–16] although the photoinduced electrons and holes can be readily quenched, in addition to undergoing recombination. For example, when n- and p-type materials are completely blended in a monolayer, the migrating electrons may be transported in the reverse direction, thereby interfering with the output current.[17] To prevent this phenomenon and to modify the surface energy, an interfacial layer (IFL) can be incorporated into the device. Conventionally, poly(3,4-ethylenedioxythiophene):polystyrenesulfonate (PEDOT:PSS)[18,19] is used, although it has some unfavorable properties,[19] including structural and electrical inhomogeneities,[20–25] facile diffusion,[22,24,26,27] and corrosive sulfonic acid groups.[28–31] Therefore, designing other potential IFL materials has become a challenge during the last decade.[32–38] 2,7-Bis(diarylamino)-5,10-dihydroindeno[2,1-*a*]indenes appear to be good bifunctional materials for use in organic light-emitting diodes (OLEDs). They exhibit sky-blue to greenish-blue fluorescence and excellent hole mobility.[39,40] Based on these results, in this study, we prepared novel interfacial materials through structural variation by incorporating *N*,*N*-di(*p*-methoxyphenyl) amine (strong electron donor) or carbazole (high hole mobility)[41–44] moieties of the 5,10-dihydroindeno[2,1-*a*]indene skeleton. Our aim was to obtain thermally evaporable small molecules that could be readily synthesized and purified and to examine their potential applications in OPVs.

Experimental

General information

All reactions of air- or moisture-sensitive compounds were performed in dry reaction vessels under a N_2 or Ar atmosphere. Analytical thin-layer chromatography (TLC) was performed on Merck 60 F254 silica gel plates, and visualization was accomplished under a UVP UVGC-25 Compact UV lamp. Fractional flash column chromatography was performed using 32–63 μm silica gel.

Materials

Compounds **1** and **2** were synthesized according to procedures described in the literature.[39,40] All reagents were purchased from Acros Organic, Sigma-Aldrich, TCI, and Alfa-Aesar and used directly without further purification. Solvents were of reagent

[a]*Department of Chemistry, Tamkang University, No. 151, Yingzhuan Rd., Tamsui Dist., New Taipei City 25137, Taiwan, Republic of China. E-mail: ywei@mail.tku.edu.tw*

[b]*Department of Materials Engineering, Ming Chi University of Technology, No. 84 Gunjuan Rd., Taishan Dist., New Taipei City 24301, Taiwan, Republic of China. E-mail: cpchen@mail.mcut.edu.tw*

[c]*Battery Research Center of Green Energy, Ming Chi University of Technology, 84 Gunjuan Road, Taishan, New Taipei City, 24301, Taiwan*

† Electronic supplementary information (ESI) available. See DOI: 10.1039/c4ra11696h

Published on 10 December 2014. Downloaded by Tamkang University Libraries on 19/01/2015 03:58:08.

grade, unless mentioned otherwise, and diethyl ether and toluene were dried over Na/benzophenone-ketyl.

Characterization

^{1}H and ^{13}C NMR spectra of solutions in CD_2Cl_2 were recorded using a Bruker AVANCE III HD spectrometer (600 MHz for ^{1}H; 150 MHz for ^{13}C) with tetramethylsilane or CH_2Cl_2 as the internal reference. Chemical shifts (δ) and coupling constants (J) are reported in ppm and Hz, respectively. Splitting patterns are described as follows: doublet, d; triplet, t; quartet, q; multiplet, m. Mass spectra and high-resolution mass spectra were recorded using LCQ Advantage GC/LC/MS and Finnigan MAT 95S spectrometers.

Steady state photophysical measurements

Absorption spectra of the solutions in spectrophotometric-grade CH_2Cl_2 were measured using a Thermo Scientific Evolution 60S spectrophotometer.

Cyclic voltammetry (CV)

CV experiments for solutions in CH_2Cl_2 were performed using a CHI 611D electrochemical analyzer with ferrocene as an internal ref. 45. Tetrabutylammonium perchlorate (0.1 M) was the supporting electrolyte. Platinum, carbon, and Ag/AgCl electrodes were used as the counter, working, and reference electrodes, respectively.

Differential scanning calorimetry (DSC)

DSC analyses were performed using a Mettler Toledo DSC 1 differential scanning calorimeter. The sample was heated (10 °C min^{-1}) to the melt and then cooled rapidly using liquid N_2. The melting point (T_m) was obtained during the first heating scan. The glass transition temperature (T_g) was recorded during the second heating scan (10 °C min^{-1}).

Thermogravimetric analyses (TGA)

TGA was performed using a PerkinElmer Pyris 1 TGA thermogravimetric analyzer. The decomposition temperature (T_d) was recorded as the temperature at which 5% weight loss occurred during the heating process (10 °C min^{-1}).

5,5,10,10-Tetraphenyl-5,10-dihydroindeno[2,1-*a*]indene (1).

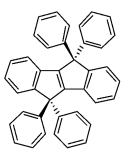

n-BuLi (1.6 M in hexane, 27.5 mL, 44 mmol) was added dropwise to a solution of (*Z*)-2,2′-dibromostilbene (6.761 g, 20 mmol) in Et_2O (100 mL) in a 250 mL, three-necked, round-bottom flask cooled to 0 °C. After stirring at this temperature for 30 min, a solution of benzophenone (8.018 g, 44 mmol) in Et_2O (20 mL) was added. The resulting mixture was gradually warmed to ambient temperature and then quenched with saturated $NaHCO_{3(aq.)}$ (50 mL). The precipitate was collected by filtration, washed with distilled water (100 mL) and hexane (100 mL), and then dried under reduced pressure. The crude residue was dissolved in AcOH (50 mL) and placed in a 100 mL, two-necked, round-bottom flask. HCl (12 N, 1 mL) was added and then the reaction mixture was heated under reflux for 2 h. After cooling to ambient temperature, saturated $NaHCO_{3(aq.)}$ (50 mL) was added and the mixture was stirred vigorously for 20 min. The yellow solid precipitate was collected by filtration, washed with distilled water (100 mL), MeOH (100 mL), and hexanes (100 mL), dried under reduced pressure, and then recrystallized (CH_2Cl_2) to afford **1** (2.441 g, 24%): T_m 376 °C (DSC); M.W.: 508.65; ^{1}H NMR (600 MHz, $CDCl_3$): δ 7.42 (dd, J = 6.8, 1.8 Hz, 2H), 7.30–7.23 (m, 20H), 7.18–7.11 (m, 6H); ^{13}C NMR (150 MHz, CD_2Cl_2): δ 157.7, 155.7, 143.0, 138.6, 128.7, 128.6, 127.4, 127.3, 126.2, 125.3, 121.1, 63.4; EI-MS (negative): calcd for $C_{40}H_{28}$ $[M]^-$: m/z 508.2, found: 508.3; TLC: R_f 0.75 (CH_2Cl_2/hexanes, 1 : 3).

2,7-Dibromo-5,5,10,10-tetraphenyl-5,10-dihydroindeno[2,1-*a*]indene (2).

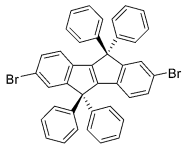

A suspension of **1** (1.017 g, 2 mmol), $CuBr_2$ (3.350 g, 15 mmol), and Al_2O_3 (10.196 g, 100 mmol) in CCl_4 (20 mL) in a 250 mL, three-necked, round-bottom flask was heated under reflux for 16 h. After cooling to ambient temperature, excess of $CuBr_2$ and Al_2O_3 were filtered through Celite. The filtrate was concentrated under reduced pressure and the residue was recrystallized (toluene) to afford **2** (1.093 g, 82%): T_m 393 °C (DSC); M.W.: 666.44; ^{1}H NMR (600 MHz, CD_2Cl_2): δ 7.54 (d, J = 1.7 Hz, 2H), 7.31–7.24 (m, 22H), 7.03 (d, J = 8.2 Hz, 2H); ^{13}C NMR (150 MHz, CD_2Cl_2): δ 159.6, 155.2, 141.8, 137.3, 130.7, 129.0, 128.7, 128.5, 127.7, 122.3, 120.4, 63.6; HR-ESI-MS (positive): calcd for $C_{40}H_{26}Br_2$ $[M^+ + H]$: m/z 667.0, found: 667.0; TLC: R_f 0.70 (CH_2Cl_2/hexanes, 1 : 3).

General procedure for Buchwald–Hartwig coupling[46,47]

A solution of **2** (666 mg, 1 mmol), $Pd_2(dba)_3$ (18 mg, 0.02 mmol), *t*-BuONa (288 mg, 3 mmol), P(*t*-Bu)$_3$ (0.03 M in toluene, 2 mL, 0.06 mmol), and a diarylamine (2.2 mmol) in toluene (20 mL) in a 25 mL, two-necked, round-bottom flask was heated under reflux for 4 h. After cooling to ambient temperature, the precipitate was collected by filtration and washed with toluene (100 mL), and the crude residue was sublimated (5×10^{-6} Torr) to afford **3a–c**.

2,7-Bis[*N*,*N*,-di(*p*-tolyl)amino]-5,5,10,10-tetraphenyl-5,10-dihydroindeno[2,1-*a*]indene (3a).

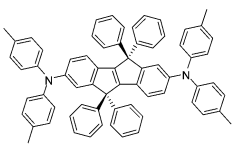

Yield: 557 mg, 62%; T_m 433 °C (DSC); T_d 514 °C (TGA); T_g 165 °C (DSC); M.W.: 899.17; ^{1}H NMR (600 MHz, CD_2Cl_2): δ 7.23

 This journal is © The Royal Society of Chemistry 2015

Published on 10 December 2014. Downloaded by Tamkang University Libraries on 19/01/2015 03:58:08.

(s, 20H), 7.15 (d, $J = 2.0$ Hz, 2H), 6.98 (d, $J = 8.3$ Hz, 8H), 6.91 (d, $J = 8.3$ Hz, 2H), 6.86 (d, $J = 8.3$ Hz, 8H), 6.65 (dd, $J = 8.3$, 2.0 Hz, 2H), 2.25 (s, 12H); ^{13}C NMR (150 MHz, CD_2Cl_2): δ 158.6, 153.8, 146.5, 145.6, 143.6, 132.9, 130.0, 128.8, 128.6, 127.1, 124.7, 121.4, 120.7, 120.4, 63.3, 20.8; TLC: R_f 0.75 (CH_2Cl_2/hexane, 1 : 3); ESI-MS (positive): calcd for $C_{64}H_{46}N_2$ $[M]^+$: m/z 898.4, found: 898.4.

2,7-Bis[*N*,*N*,-di(*p*-methoxyphenyl)amino]-5,5,10,10-tetraphenyl-5,10-dihydroindeno[2,1-*a*]indene (3b).

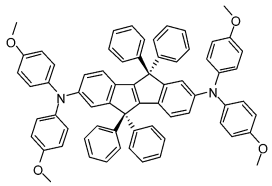

Yield: 520 mg, 54%; T_m 423 °C (DSC); T_d 474 °C (TGA); T_g 156 °C (DSC); M.W.: 963.17; ^{1}H NMR (600 MHz, CD_2Cl_2): δ 7.26–7.19 (m, 24H), 7.09 (d, $J = 7.1$ Hz, 2H), 6.80 (d, $J = 8.8$ Hz, 8H), 6.71 (d, $J = 8.8$ Hz, 8H), 3.75 (s, 12H); TLC: R_f 0.75 (CH_2Cl_2/hexane, 1 : 3); HR-ESI-MS (positive): calcd for $C_{64}H_{46}N_2$ $[M]^+$: m/z 962.4084, found: 962.4080.

2,7-Bis(*N*-carbazolyl)-5,5,10,10-tetraphenyl-5,10-dihydroindeno-[2,1-*a*]indene (3c).

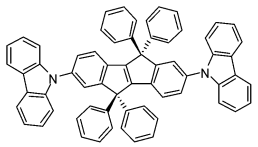

Yield: 537 mg, 64%: T_m 435 °C (DSC); T_d 546 °C (TGA); T_g 204 °C (DSC); M.W.: 839.03; ^{1}H NMR (600 MHz, CD_2Cl_2): δ 8.10 (d, $J =$ 7.8 Hz, 4H), 7.71 (s, 2H), 7.46–7.44 (m, 12H), 7.36–7.30 (m, 20H), 7.23–7.23 (m, 4H); ^{13}C NMR (150 MHz, CD_2Cl_2):δ 159.5, 142.6, 141.0, 137.5, 136.0, 129.1, 128.7, 128.7, 127.7, 126.2, 126.0, 124.2, 123.7, 122.1, 120.5, 120.3, 110.1, 63.8; TLC: R_f 0.75 (CH_2Cl_2/hexanes, 1 : 3); ESI-MS (positive): calcd for $C_{64}H_{42}N_2Na$ $[M + Na]^{2+}$: m/z 442.2, found: 442.3.

Device fabrication and measurements

All BHJ OPV cells were prepared using the following device fabrication procedure, which is similar to that described previously.[48–50] Glass/indium tin oxide (ITO) substrates [Sanyo, Japan (8 Ω $\square^{-1}$)] were sequentially patterned lithographically; cleaned with detergent; ultrasonicated in acetone and isopropyl alcohol; dried on a hot plate at 140 °C for 10 min; and treated with oxygen plasma for 5 min. For the normal cell, PEDOT:PSS (Baytron P-VP AI4083) was passed through a 0.45 μm filter prior to being deposited on ITO (thickness: *ca.* 30 nm) through spin-coating at 3000 rpm in air, and the sample was then dried at 140 °C for 20 min inside a glove box. For the novel cell structure, **3a**, **3b**, or **3c** was thermally evaporated on ITO and subjected to various post-annealing conditions. A blend of poly(3-hexylthiophene-2,5-diyl) (P3HT) and [6,6]-phenyl-C_{61}-butyric acid methyl ester (PCBM) at a defined ratio of 1 : 0.9 was stirred overnight in *o*-dichlorobenzene (*o*-DCB), filtered through a 0.2 μm polytetrafluoroethylene (PTFE) filter, and then spin-coated (450 rpm, 30 s; then 1000 rpm, 1 s) on top of the HTM layer. The device was completed by depositing a 30 nm thick layer of Ca and a 100 nm thick layer of Al at pressures of less than 10^{-6} Torr. The active area of each device was 10 mm^2. The current–voltage (*I–V*) properties of the devices were measured using a computer-controlled Keithley 2400 source measurement unit (SMU) and a Newport solar simulator (Oriel® Sol2A Class ABA Solar Simulators) under AM 1.5 illumination (100 mW cm^{-2}). The illumination intensity was calibrated using a standard Si reference cell and a KG-5 filter. The morphologies of the polymer films were analyzed through atomic force microscopy (AFM) using a VEECO DICP-II instrument operated in the dynamic force mode at ambient temperature; moreover, the etched Si probe exhibited a resonant frequency of 131 kHz and a spring constant of 11 N m^{-1}. Surface energies were determined through contact angle goniometry using the well-established Fowkes method.[38,51] The contact angles of DI H_2O and CH_2I_2 were used to calculate the dispersion and polar components of the derived films. The substrate surface energies were calculated using CH_2I_2 ($\gamma^d = 48.5$ mJ m^{-2}; $\gamma^p = 2.3$ mJ m^{-2}) and water ($\gamma^d = 21.8$ mJ m^{-2}; $\gamma^p = 51.0$ mJ m^{-2}) as probe liquids.[38]

Results and discussion

As illustrated in Scheme 1, we synthesized and purified compounds **1–3** in good yield; moreover, their NMR spectra were consistent with their proposed molecular structures. Because of their rigid structures, our target molecules **3a–c** exhibited excellent thermal stabilities; moreover, their T_g, T_m, and T_d values were in the range of 165–204, 393–435, and 474–546 °C, respectively (Table 1). Notably, they are minimally soluble in common organic solvents with solubilities in *o*-DCB of less than 10^{-2} mM; moreover, this characteristic facilitated morphological control during the deposition of the active layer through spin-coating, thereby avoiding mixing between the interfaces. We estimated the energy levels of the highest occupied molecular orbital (HOMO) and lowest unoccupied molecular orbital (LUMO) of **3a–c** from their absorption spectra

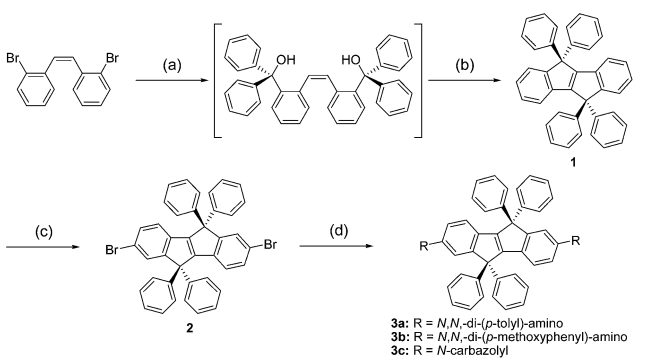

Scheme 1 Synthetic strategy for **1–3**. Reagents and conditions: (a) *n*-BuLi and benzophenone, Et_2O, 0 °C, 2 h. (b) cat. HCl, AcOH, reflux, 4 h. (c) $CuBr_2/Al_2O_3$, CCl_4, reflux, 18 h. (d) $Pd_2(dba)_3$, P(*t*-Bu)$_3$, *t*-BuONa, diarylamine, toluene, reflux, 4 h.

Published on 10 December 2014. Downloaded by Tamkang University Libraries on 19/01/2015 03:58:08.

Table 1 Photophysical and electrochemical data for **3a–c**

	Abs. λ_{max}[a,b] (nm)	$T_g/T_m/T_d$ (°C)	E_{ox}[a] (V)
3a	310 (19.7), 410 (34.2), 427 (33.1)	165/433/514	−0.01, +0.21
3b	305 (22.2), 414 (38.8), 429 (38.2)	156/423/474	−0.02, +0.30
3c	294 (26.9), 370 (37.7), 385 (31.6)	204/435/546	+0.69, +0.86

[a] Measured in CH_2Cl_2. [b] Data in parentheses correspond to $\varepsilon \times 10^{-3}$.

(Fig. 1) and oxidation potentials. For comparison, the absorption spectra for PEDOT:PSS are shown in Fig. S1a.† Upon photoexcitation at ambient temperature, the maximum absorption peaks (abs. λ_{max}) followed the order **3b** (429 nm) ≈ **3a** (427 nm) > **3c** (385 nm). Notably, this order, which represents the relative electron donating characteristics of the various diarylamino groups, is consistent with the oxidation behavior evaluated using CV. The first oxidation potentials (E_{ox}) of **3a–c** were all observed as reversible redox couples at −0.01, +0.02, and +0.69 V, respectively (Fig. S2†). Compound **3b** has the lowest value of E_{ox} because of its two *p*-MeO substituents on each diphenylamino unit. On the other hand, the anti-aromaticity of a carbazole unit tends to localize electrons; therefore, **3c** exhibited the highest value of E_{ox}. Fig. 2 presents energy diagrams for the heterojunctions (HJs) of these OPVs. The energy levels of **3a–c** fulfil the requirements for an HTM to be used in an OPV. The HOMO energy levels of **3a–c** (−4.79, −4.82, and −5.49 eV, respectively) agree well with the work function of ITO (−4.7 eV) and may facilitate hole transfer from P3HT (HOMO energy level: −5.0 eV) to ITO. Furthermore, the LUMO energy levels of **3a–c** (−2.09, −2.03, and −2.50 eV, respectively) are higher than that of PCBM (−3.7 eV), thereby decreasing the possibility of charge recombination at the interface. As a result, we expected devices embedded with **3a–c** to display good to excellent performance.

We spin-coated a P3HT:PCBM blend solution onto the surfaces of the substrates coated with the various hole transporting layers (HTLs) to form the active layers of our OPV devices. The physical properties of the underlay film (in this study, the various HTLs), including the surface roughness and topographic properties[52–54] and the surface energy[55–58] as

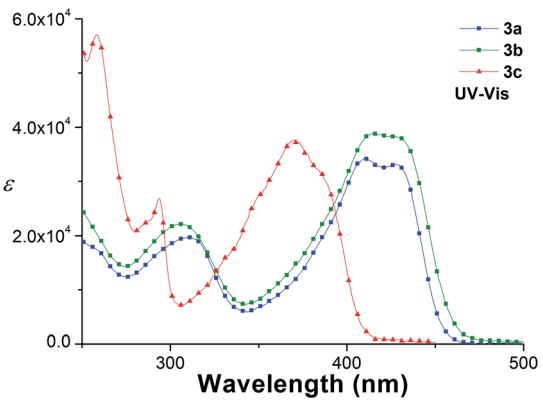

Fig. 1 Stacked plots of the absorption spectra of **3a–c**.

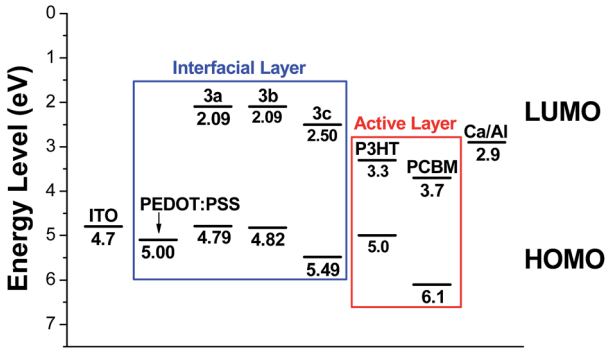

Fig. 2 Energy levels of **3a–c** and relevant OPV materials.

intrinsic material characteristics,[59,60] can influence the morphology of the active layer, and hence the performance of the resulting device.[61,62] In the optimal morphology, the donor and acceptor must be blended to increase the interfacial areas between them while maintaining a certain degree of phase separation between the donor and acceptor domains to enable the requisite bicontinuous structure throughout the BHJ layer. Charge collection for the normal OPV device can be enhanced through vertical phase separation with a donor-enriched bottom surface and an acceptor-enriched top surface.[52,54] To investigate how the morphologies of our HTL films of **3a–c** evolved in response to various deposition conditions and hence to determine the morphologies of the active layers, we employed AFM in the tapping mode to characterize their topographies. For direct comparison, we prepared these films for AFM analysis under the same conditions that we used for device fabrication. AFM analysis revealed that the thickness of each HTL film was approximately 10 nm. Fig. 3 displays the topographies of our HTL films. The surfaces of the as-prepared layers of **3a–c** were fairly smooth, with root mean square (RMS) roughnesses of 2.5, 2.4, and 2.5 nm, respectively. These films appeared to have amorphous-like morphologies rather than crystalline forms. For direct comparison, we also prepared a PEDOT:PSS

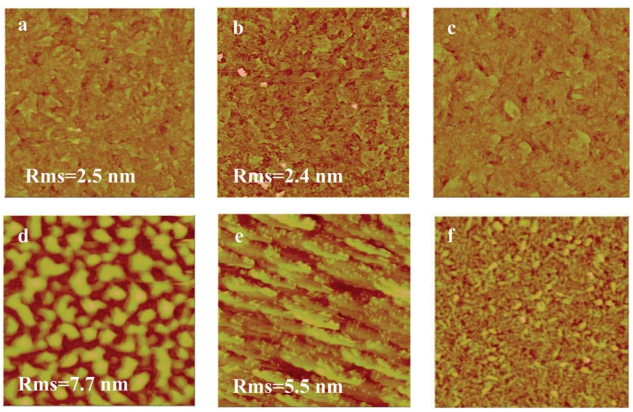

Fig. 3 AFM topographical images (5 μm × 5 μm) of (a–c) as-deposited and (d–f) annealed (200 °C, 10 min) films of (a and d) **3a**, (b and e) **3b**, and (c and f) **3c**.

This journal is © The Royal Society of Chemistry 2015

Published on 10 December 2014. Downloaded by Tamkang University Libraries on 19/01/2015 03:58:08.

film under the same conditions. Its AFM image showed that the RMS of PEDOT:PSS was 2 nm (Fig. S1b†). Because the crystallinity, morphology, and carrier mobility of an organic film can be manipulated through thermal annealing,[63,64] we studied the effects of thermal annealing, at temperatures greater than their T_g values, on the morphological evolution of our HTLs. Fig. S3† presents AFM images of films of **3a**, **3b** and **3c**, which had been annealed at 160 °C for 10 min. We observed an amorphous-like morphology for **3a**, similar to that of its as-deposited film. After thermal annealing at 160 °C, the films of **3b** and **3c** possessed a rather homogeneous morphology with well-distributed domains of equally sized crystallites. When we annealed these HTL films at a higher temperature of 200 °C (close to the value of T_g of **3c**) for 10 min, we observed dramatic changes in their morphologies. The surfaces of the films of **3a**, **3b** and **3c** after annealing at 200 °C had become rougher with RMS roughnesses of 7.7, 4.5, and 5.5 nm, respectively; in addition, they featured well-defined pebble-, long rod-, and dot/rod-like crystallites, respectively (Fig. 3d–f). Thus, the morphologies of these HTLs changed from smooth/amorphous to rougher topographies, with associated well-defined crystallinity, after we applied thermal treatment at an appropriate temperature. From the AFM images, we conclude that enhanced crystallization of **3a–3c** occurred at the high annealing temperature. It is well established that a thin film exhibiting high carrier mobility should contain active materials of high crystallinity.[65] Accordingly, we suspected that devices incorporating our thermally annealed HTLs might exhibit improved OPV performance as a result of superior carrier transport. We fabricated OPV devices by spin-coating blends of P3HT and PCBM (D/A), at a weight ratio of 1 : 0.9, from *o*-DCB solutions onto our HTLs. We studied the surface morphologies of the P3HT:PCBM blend films on these HTLs, as well as on the PEDOT:PSS (Fig. S4†), using the same fabrication conditions. Substituting our HTLs for PEDOT:PSS in the OPV devices had a significant effect on the surface morphologies of the blend films. The RMS roughnesses of the blend films on the as-deposited films of **3a–c** were 23.8, 24.6, and 28.9 nm, respectively. A smoother surface topography, with little phase segregation, appeared for the PEDOT:PSS-derived blend film. We observed greater phase segregation of the P3HT:PCBM blends, associated with greater RMS roughness, on our HTL-derived blends. Fig. S2d–f† show the AFM images of the corresponding blends on the HTL films of **3a–c**, which we had annealed at 200 °C; moreover, the RMS roughnesses were 7.8, 8.3, and 16.2 nm, respectively. In comparison with the blends on the as-deposited HTLs, these films had smoother topographies, associated with lower degrees of phase segregation. Thus, these topographic images revealed that substituting the novel HTLs in place of the PEDOT:PSS layer had a significant effect on the morphologies of the films, presumably altering the OPV performance.

Cho's group investigated the relationship between the active layer morphology of a BHJ and the surface energies of various underlayers.[57] They found that the photocurrent of an OPV device can be increased by optimizing the BHJ morphology, mediated by the surface energy of self-assembled monolayer-modified ZnO. They observed improvements in the power conversion efficiency (PCE) of the devices over a specific range of surface energies. To investigate how the morphologies of the blend films evolved with respect to the surface energies, we used contact angle goniometry and Fowkes model to calculate the surface energies of our HTLs.[51] We determined the surface energies of the HTLs by measuring their contact angles with distilled H_2O and CH_2I_2 as probe liquids and employing the geometric mean equation,

$$(1 + \cos\theta)\gamma_{pl} = 2(\gamma_s^d\gamma_{pl}^d)^{1/2} + 2(\gamma_s^p\gamma_{pl}^p)^{1/2}$$

where γ_s and γ_{pl} are the surface energies of the sample and probe liquid, respectively, and the superscripts d and p represent the dispersion ($\gamma_{dispersive}$) and polar (γ_{polar}) components of the surface energy, respectively. Table S1† lists the dispersive and polar components and the total surface (γ_{total}) energies of the films of **3a–c**. The surface energies (γ_{total}) of the as-cast films of **3a–c** were 58.2, 54.4. and 60.8 mN m^{-1}, respectively. A close look at Fig. S4† reveals overall rougher morphologies, with large degrees of phase segregation, for the blend films prepared on the as-cast HTLs. The surface energies of films of **3a–c** that had been treated at 200 °C were 52.1, 52.7, and 58.6 mN m^{-1}, respectively, *i.e.*, thermal treatment decreased the surface energy of these films. The blend films on these thermally treated HTLs displayed finer phase-separated blend structures, associated with small phase-aggregation domains. The films of **3a** and **3b** had the lowest surface energies, and their blend films exhibited the lowest RMS roughness and related finer morphologies. The surface energy naturally varies in relation to the intrinsic properties of a material and its interfacial status and can have its own impact on an investigated system.[57] Our results suggest that the surface energy of the HTL plays a significant role during the formation of the BHJ by affecting its phase-segregation process.

We fabricated OPVs, having the layered configuration glass/ITO/HTLs/P3HT:PCBM/Ca/Al, using methods similar to those we have reported previously.[48–50] The layers of Ca (30 nm) and Al (100 nm) were deposited thermally under vacuum. The optimal performance of our devices occurred when depositing P3HT/PCBM blend from a solution at a concentration of 33.3 mg mL^{-1} (in total) in *o*-DCB at a spin-coating rate of 450 rpm for 30 s and then at 1000 rpm for 1 s. Fig. 4 presents the *J–V* curves of the OPVs incorporating our various HTL layers. Table 1 summarizes the open circuit voltages (V_{oc}), current densities (J_{sc}), fill factor (FFs), and PCEs of the devices we prepared with an optimal active layer thickness of 180 nm. The PCEs of these fabricated devices were reproducible, with only small variations exhibited among eight individual OPV devices. When we varied the thicknesses of our 5,10-dihydroindeno[2,1-*a*]indene-based HTLs, we found that the optimal thickness was approximately 10 nm. Compared to the device prepared without an HTL layer, the PCE of the **3a**-based optimized device was significantly higher, primarily due to increase in the values of both J_{sc} and the FF. The PCE of the optimized device improved from 1.0% to 2.0% after incorporating **3a** as the HTL. This trend in performance can be explained by considering the energy level of each

Published on 10 December 2014. Downloaded by Tamkang University Libraries on 19/01/2015 03:58:08.

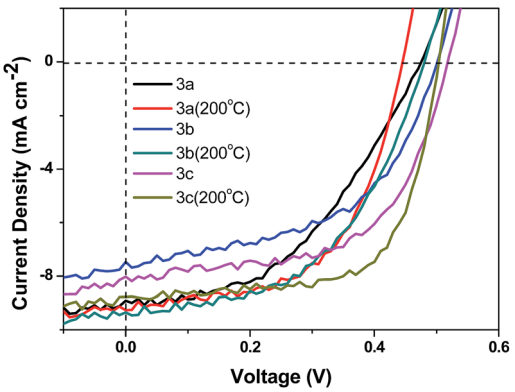

Fig. 4 Current density–potential characteristics of devices under illumination with AM 1.5G solar simulated light (100 mW cm^{-2}).

layer. In the absence of an HTL layer, ITO served as an electrode with the electrons and holes reaching the ITO freely. As a result, the device functioned poorly as a diode and hence displayed poor values of FF and J_{sc}. The p-type properties and HOMO energy level of **3a** agree well with the work function of ITO and the facilitated hole transfer from P3HT (HOMO energy level: −5.0 eV) to ITO. The LUMO energy level of **3a** (−2.0 eV) is higher than that of PCBM (−3.7 eV), thereby decreasing the likelihood of interfacial charge recombination. Thus, the film of **3a** served as an electron-blocking layer (EBL) and HTL, promoting hole extraction from the active layer into the anode while simultaneously preventing electrons from traversing the HTL without significant radiative recombination, thereby greatly increasing the efficiency of the device. We observed similar results for the devices incorporating films of **3b** and **3c**. The highest PCE (2.4% ± 0.1%) was that of the **3c**-containing device, which exhibited a J_{sc} value of 7.8 ± 0.5 mA cm^{-2}, a V_{oc} value of 0.50 ± 0.02 V, and a FF of 58.4% ± 0.4% (Table 2 and Fig. 4). The increase in PCE from 2.0% to 2.4% arose primarily from increase in the values of V_{oc} and the FF. The improvement in the value of V_{oc} resulted from the deep HOMO energy level of **3c**. We calculated the series resistances (R_s) and shunt resistances (R_{sh}) from the inverse slopes of the *J*–*V* curves. As displayed in Table 1, the **3c**-containing device exhibited the smallest R_s value, indicating that the bulk resistance of this device was the lowest. A significant increase in the value of R_{sh}, for the **3a**–**3c** devices, from 199 to 315 Ω cm^2, indicates that the defects were responsible for charge recombination and that the leakage current was the lowest for the device incorporating **3c**. On the other hand, because 5,5,10,10-tetraphenyl-5,10-dihydroindeno[2,1-*a*]indene has a planar framework,[39] the extent of hole transport is related to the twisting angles between the central bridge and both flanking sides. According to simulations, the diarylamino groups in **3a–c** are tilted by 68.5° ± 1.4°, 68.3° ± 0.8°, and approximately 54.6°, respectively (Fig. S5†). From these values, we might expect that **3c** would exhibit the highest mobility, and hence provide the device displaying the best performance under similar device fabrication conditions. From AFM images of the morphologies of these HTLs and their corresponding active layers (Fig. 3 and S2†), we attribute the enhancement in FF to the relatively high coplanarity of **3c** and its corresponding greater hole transporting ability. Compared to the devices incorporating the as-deposited HTLs, the devices containing the HTLs that had been annealed at 200 °C exhibited improved device performances. The best OPV performance was that of the device incorporating the film of **3c** that had been thermally treated at 200 °C; this device exhibited a PCE of 2.6 ± 0.4%, a J_{sc} value of 8.5 ± 0.4 mA cm^{-2}, a V_{oc} value of 0.50 ± 0.02 V, and a FF of 63.8% ± 4.0%. The increase in PCE was due to enhancements in the values of J_{sc} and FF, which were associated with the lower value of R_s and the higher value of R_{sh}. This trend in performance can be explained by considering the morphological properties of the blends and the crystallinity of the HTLs. Thermal annealing allowed the HTL to improve its crystalline morphology, and hence increase the degree of charge transport in the device. The relatively higher J_{sc} value of the annealed-film device appeared to be related to its smaller phase-separated domains, which provided a greater interfacial area for exciton dissociation; as a result, its current density increased by approximately 4% to 13%. The J_{sc} value of the device incorporating the film of **3c** that had been annealed at 200 °C was lower than that of the other devices, presumably because of its rougher surface morphology (Fig. S3†). Apart from the morphology of the active layer, we suspect that the hole mobility of the devices using various HTLs also contributes to variations in device performance. To evaluate the contribution of hole mobility, we employed hole-only devices using a high-work-function material such as gold (Au) as the cathode to block

Table 2 PV parameters of OPV devices prepared using various fabrication conditions

Devices	J_{sc} (mA cm^{-2})	V_{oc} (V)	FF (%)	η (%)	η^c (%)	$R_s{}^d$	$R_{sh}{}^d$
w/o HTL	7.4 ± 0.1	0.37 ± 0.05	30.0 ± 2.0	0.8 ± 0.2	1.0	6.7	68
P[a]	9.6 ± 0.3	0.59 ± 0.03	56.9 ± 2.0	3.5 ± 0.2	3.7	5.2	680
3a	8.5 ± 0.6	0.46 ± 0.04	43.3 ± 2.0	1.7 ± 0.3	2.0	11.7	199
3a[b]	8.5 ± 0.8	0.47 ± 0.03	50.1 ± 5.5	2.0 ± 0.3	2.3	6.7	310
3b	7.6 ± 0.5	0.47 ± 0.04	51.3 ± 2.0	1.9 ± 0.2	2.1	13.3	212
3b[b]	8.5 ± 0.7	0.44 ± 0.04	50.0 ± 0.4	2.0 ± 0.3	2.3	10.7	254
3c	7.8 ± 0.5	0.50 ± 0.02	58.4 ± 0.4	2.4 ± 0.1	2.5	5.5	315
3c[b]	8.5 ± 0.4	0.50 ± 0.02	63.8 ± 4.0	2.6 ± 0.4	3.0	3.6	526

[a] PEDOT:PSS. [b] After thermal evaporation of the HTLs, the films were subjected to thermal annealing at 200 °C for 10 min inside a glove box. [c] PCE of the best device. [d] Unit: Ω cm^2.

 This journal is © The Royal Society of Chemistry 2015

Published on 10 December 2014. Downloaded by Tamkang University Libraries on 19/01/2015 03:58:08.

the back injection of electrons. When a sufficient voltage is applied to this hole-only device, the transport of holes through the active layer film is limited by the accumulated space charge. The space charge limited current (SCLC) is described by the equation:

$$J = \frac{9}{8}\varepsilon_r\varepsilon_0\mu_h\frac{V^2}{L^3}$$

where ε_r is the dielectric constant of the polymer, ε_0 is the permittivity of free space, μ_h is the hole mobility, V is the voltage applied to the device, and L is the blend thickness.[48] Fig. S6† displays the experimental dark-current densities measured in the hole-only devices. The applied voltage (V_{appl}) was corrected for the built-in voltage (V_{bi}), which is due to the difference in the work function or HOMO energy levels of the anodes (HTLs) and the cathode (Au). The plots of $J^{0.5}$ *versus* $V_{appl} - V_{bi}$ for each device were nearly a straight line, providing a slope that we used to calculate the field-independent mobility of the blend films. The field-independent mobilities of the devices incorporating various HTLs of PEDOT:PSS, **3a**, **3b** and **3c** were 2.0×10^{-8}, 3.9×10^{-9}, 4.6×10^{-8} and 5.3×10^{-9} $m^2\ V^{-1}\ s^{-1}$, respectively. The highest mobility is observed for **3c**-derived devices. This suggested that the enhanced PCE of the **3c**-derived device was due to the higher hole mobility. Compared to the device fabricated from PEDOT:PSS, we observed a decrease in PCE from 3.7% to 3.0% because of the V_{oc} value. There remains considerable room for improvement in the performance of such devices through optimization of their morphologies and architectures. We anticipate that high-performance OPV cells could be obtained by optimizing the molecular structures.

Conclusions

In an attempt to optimize their molecular design, we synthesized several thermally evaporable 2,7-bis(diarylamino)-5,10-dihydroindeno[2,1-*a*]indene derivatives and examined them for OPV applications. The extremely poor solubilities of these compounds facilitated device fabrication through spin-coating. Substituting these materials as HTLs in place of a PEDOT:PSS layer significantly affected the morphology of the blend films deposited upon them and altered the OPV performance. We have found that the surface energies, surface roughnesses, and intrinsic properties of the HTLs all played significant roles, affecting the formation and morphology of the BHJ by influencing the phase-segregation process. The maximum values of J_{sc}, V_{oc}, and PCE, which are 8.8 mA cm^{-2}, 0.50 V, and 3.0%, respectively, were found for the device incorporating a film of **3c** that had been annealed at 200 °C. Moreover, this device exhibited a remarkable FF of 67.8% (*cf.* a value of 58.9% for the corresponding device containing PEDOT:PSS). Thus, **3c** appears to be one of the best small-molecule HTMs prepared to date.

Acknowledgements

This research was sponsored by the Ministry of Science and Technology of Taiwan (101-2113-M-032-008-MY2; 101-2113-M-131-001-MY2), Kohan Instruments Co., Ltd., and Tamkang University.

Notes and references

1 R. F. Service, *Science*, 2005, **309**, 548–551.
2 J. Potočnik, *Science*, 2007, **315**, 810–811.
3 J. Franck and E. G. Dymond, *Trans. Faraday Soc.*, 1926, **21**, 536–542.
4 E. Condon, *Phys. Rev.*, 1926, **28**, 1182–1201.
5 F. C. Krebs, N. Espinosa, M. Hösel, R. R. Søndergaard and M. Jørgensen, *Adv. Mater.*, 2014, **26**, 29–39.
6 N. Espinosa, F. O. Lenzmann, S. Ryley, D. Angmo, M. Hosel, R. R. Sondergaard, D. Huss, S. Dafinger, S. Gritsch, J. M. Kroon, M. Jorgensen and F. C. Krebs, *J. Mater. Chem. A*, 2013, **1**, 7037–7049.
7 J. E. Carlé, T. R. Andersen, M. Helgesen, E. Bundgaard, M. Jørgensen and F. C. Krebs, *Sol. Energy Mater. Sol. Cells*, 2013, **108**, 126–128.
8 Y. Galagan, E. W. C. Coenen, B. Zimmermann, L. H. Slooff, W. J. H. Verhees, S. C. Veenstra, J. M. Kroon, M. Jorgensen, F. C. Krebs and R. Andriessen, *Adv. Energy Mater.*, 2014, **4**, 1300498.
9 N. Espinosa, M. Hosel, M. Jorgensen and F. C. Krebs, *Energy Environ. Sci.*, 2014, **7**, 855–866.
10 T. R. Andersen, H. F. Dam, M. Hosel, M. Helgesen, J. E. Carle, T. T. Larsen-Olsen, S. A. Gevorgyan, J. W. Andreasen, J. Adams, N. Li, F. Machui, G. D. Spyropoulos, T. Ameri, N. Lemaitre, M. Legros, A. Scheel, D. Gaiser, K. Kreul, S. Berny, O. R. Lozman, S. Nordman, M. Valimaki, M. Vilkman, R. R. Sondergaard, M. Jorgensen, C. J. Brabec and F. C. Krebs, *Energy Environ. Sci.*, 2014, **7**, 2925–2933.
11 Z. A. Tan, S. S. Li, F. Z. Wang, D. P. Qian, J. Lin, J. H. Hou and Y. F. Li, *Sci. Rep.*, 2014, **4**, 4691–4700.
12 C. Cui, W.-Y. Wong and Y. Li, *Energy Environ. Sci.*, 2014, **7**, 2276–2284.
13 X. Li, W. C. H. Choy, L. Huo, F. Xie, W. E. I. Sha, B. Ding, X. Guo, Y. Li, J. Hou, J. You and Y. Yang, *Adv. Mater.*, 2012, **24**, 3046–3052.
14 J. J. M. Halls, C. A. Walsh, N. C. Greenham, E. A. Marseglia, R. H. Friend, S. C. Moratti and A. B. Holmes, *Nature*, 1995, **376**, 498–500.
15 G. Yu, J. Gao, J. C. Hummelen, F. Wudl and A. J. Heeger, *Science*, 1995, **270**, 1789–1791.
16 X. Li, W. C. H. Choy, F. Xie, S. Zhang and J. Hou, *J. Mater. Chem. A*, 2013, **1**, 6614–6621.
17 H.-J. Wang, C.-W. Chou, C.-P. Chen, Y.-H. Chen, R.-H. Lee and R.-J. Jeng, *J. Mater. Chem. A*, 2013, **1**, 8950.
18 A. Elschner, F. Bruder, H. W. Heuer, F. Jonas, A. Karbach, S. Kirchmeyer, S. Thurm and R. Wehrmann, *Synth. Met.*, 2000, **111–112**, 139–143.
19 C.-P. Chen, Y.-D. Chen and S.-C. Chuang, *Adv. Mater.*, 2011, **23**, 3859–3863.
20 P. E. Burrows, V. Bulovic, S. R. Forrest, L. S. Sapochak, D. M. McCarty and M. E. Thompson, *Appl. Phys. Lett.*, 1994, **65**, 2922–2924.

Published on 10 December 2014. Downloaded by Tamkang University Libraries on 19/01/2015 03:58:08.

21 N. R. Armstrong, C. Carter, C. Donley, A. Simmonds, P. Lee, M. Brumbach, B. Kippelen, B. Domercq and S. Yoo, *Thin Solid Films*, 2003, **445**, 342–352.
22 M. Kemerink, S. Timpanaro, M. M. de Kok, E. A. Meulenkamp and F. J. Touwslager, *J. Phys. Chem. B*, 2004, **108**, 18820–18825.
23 S.-I. Na, S.-S. Kim, J. Jo and D.-Y. Kim, *Adv. Mater.*, 2008, **20**, 4061–4067.
24 L. S. C. Pingree, B. A. MacLeod and D. S. Ginger, *J. Phys. Chem. C*, 2008, **112**, 7922–7927.
25 A. W. Hains, J. Liu, A. B. F. Martinson, M. D. Irwin and T. J. Marks, *Adv. Funct. Mater.*, 2010, **20**, 595–606.
26 M. Brumbach, P. A. Veneman, F. S. Marrikar, T. Schulmeyer, A. Simmonds, W. Xia, P. Lee and N. R. Armstrong, *Langmuir*, 2007, **23**, 11089–11099.
27 A. M. Nardes, M. Kemerink, R. A. J. Janssen, J. A. M. Bastiaansen, N. M. M. Kiggen, B. M. W. Langeveld, A. J. J. M. van Breemen and M. M. de Kok, *Adv. Mater.*, 2007, **19**, 1196–1200.
28 M. Jørgensen, K. Norrman and F. C. Krebs, *Sol. Energy Mater. Sol. Cells*, 2008, **92**, 686–714.
29 W. Tang, V. Chellappan, M. Liu, Z.-K. Chen and L. Ke, *ACS Appl. Mater. Interfaces*, 2009, **1**, 1467–1473.
30 M. Fujitsuka, D. W. Cho, H.-H. Huang, J.-S. Yang and T. Majima, *J. Phys. Chem. B*, 2011, **115**, 13502–13507.
31 M. Manceau, A. Rivaton, J.-L. Gardette, S. Guillerez and N. Lemaître, *Sol. Energy Mater. Sol. Cells*, 2011, **95**, 1315–1325.
32 S. p. Berny, L. Tortech, M. Véber and D. Fichou, *ACS Appl. Mater. Interfaces*, 2010, **2**, 3059–3068.
33 A. W. Hains, Z. Liang, M. A. Woodhouse and B. A. Gregg, *Chem. Rev.*, 2010, **110**, 6689–6735.
34 R. Steim, F. R. Kogler and C. J. Brabec, *J. Mater. Chem.*, 2010, **20**, 2499–2512.
35 A. W. Hains, C. Ramanan, M. D. Irwin, J. Liu, M. R. Wasielewski and T. J. Marks, *ACS Appl. Mater. Interfaces*, 2009, **2**, 175–185.
36 M. D. Irwin, J. Liu, B. J. Leever, J. D. Servaites, M. C. Hersam, M. F. Durstock and T. J. Marks, *Langmuir*, 2009, **26**, 2584–2591.
37 S. W. Shelton, T. L. Chen, D. E. Barclay and B. Ma, *ACS Appl. Mater. Interfaces*, 2012, **4**, 2534–2540.
38 C. K. Song, A. C. White, L. Zeng, B. J. Leever, M. D. Clark, J. D. Emery, S. J. Lou, A. Timalsina, L. X. Chen, M. J. Bedzyk and T. J. Marks, *ACS Appl. Mater. Interfaces*, 2013, **5**, 9224–9240.
39 P. Y. Shen, S. H. Wu, Y. T. Huang and Y. Wei, *Res. Chem. Intermed.*, 2014, **40**, 2199–2205.
40 Y. Wei, W.-J. Wang, Y.-T. Huang, B.-C. Wang, W.-H. Chen, S.-H. Wu and C.-H. He, *J. Phys. Chem. C*, 2014, **2**, 1779–1782.
41 B. Xu, E. Sheibani, P. Liu, J. Zhang, H. Tian, N. Vlachopoulos, G. Boschloo, L. Kloo, A. Hagfeldt and L. Sun, *Adv. Mater.*, 2014, **26**, 6629–6634.
42 J. C. Ribierre, T. Aoyama, T. Muto, Y. Imase and T. Wada, *Org. Electron.*, 2008, **9**, 396–400.
43 E. Bellmann, S. E. Shaheen, R. H. Grubbs, S. R. Marder, B. Kippelen and N. Peyghambarian, *Chem. Mater.*, 1999, **11**, 399–407.
44 M. Tamada, H. Koshikawa, T. Suwa, T. Yoshioka, H. Usui and H. Sato, *Polymer*, 2000, **41**, 5661–5667.
45 G. Gritzner and J. Kuta, *Pure Appl. Chem.*, 1984, **56**, 461–466.
46 A. S. Guram, R. A. Rennels and S. L. Buchwald, *Angew. Chem., Int. Ed. Engl.*, 1995, **34**, 1348–1350.
47 J. Louie and J. F. Hartwig, *Tetrahedron Lett.*, 1995, **36**, 3609–3612.
48 C.-P. Chen and H.-L. Hsu, *Macromol. Rapid Commun.*, 2013, **34**, 1623–1628.
49 C.-P. Chen, Y.-C. Chen and C.-Y. Yu, *Polym. Chem.*, 2013, **4**, 1161–1166.
50 H.-L. Hsu, C.-P. Chen, J.-Y. Chang, Y.-Y. Yu and Y.-K. Shen, *Nanoscale*, 2014, **6**, 10281.
51 K.-J. Chang, F.-Y. Yang, C.-C. Liu, M.-Y. Hsu, T.-C. Liao and H.-C. Cheng, *Org. Electron.*, 2009, **10**, 815–821.
52 A. K. K. Kyaw, D. H. Wang, V. Gupta, J. Zhang, S. Chand, G. C. Bazan and A. J. Heeger, *Adv. Mater.*, 2013, **25**, 2397–2402.
53 Y. Zhou, C. Fuentes-Hernandez, J. Shim, J. Meyer, A. J. Giordano, H. Li, P. Winget, T. Papadopoulos, H. Cheun, J. Kim, M. Fenoll, A. Dindar, W. Haske, E. Najafabadi, T. M. Khan, H. Sojoudi, S. Barlow, S. Graham, J.-L. Brédas, S. R. Marder, A. Kahn and B. Kippelen, *Science*, 2012, **336**, 327–332.
54 C.-Y. Chang, Y.-J. Cheng, S.-H. Hung, J.-S. Wu, W.-S. Kao, C.-H. Lee and C.-S. Hsu, *Adv. Mater.*, 2012, **24**, 549–553.
55 Y. Sun, S.-C. Chien, H.-L. Yip, K.-S. Chen, Y. Zhang, J. A. Davies, F.-C. Chen, B. Lin and A. K. Y. Jen, *J. Mater. Chem.*, 2012, **22**, 5587–5595.
56 A. C. Arias, N. Corcoran, M. Banach, R. H. Friend, J. D. MacKenzie and W. T. S. Huck, *Appl. Phys. Lett.*, 2002, **80**, 1695–1697.
57 X. Bulliard, S.-G. Ihn, S. Yun, Y. Kim, D. Choi, J.-Y. Choi, M. Kim, M. Sim, J.-H. Park, W. Choi and K. Cho, *Adv. Funct. Mater.*, 2010, **20**, 4381–4387.
58 D. O. Hutchins, T. Weidner, J. Baio, B. Polishak, O. Acton, N. Cernetic, H. Ma and A. K. Y. Jen, *J. Phys. Chem. C*, 2013, **1**, 101–113.
59 Y.-J. Cheng, C.-H. Hsieh, Y. He, C.-S. Hsu and Y. Li, *J. Am. Chem. Soc.*, 2010, **132**, 17381–17383.
60 S. Khodabakhsh, B. M. Sanderson, J. Nelson and T. S. Jones, *Adv. Funct. Mater.*, 2006, **16**, 95–100.
61 J. H. Park, T.-W. Lee, B.-D. Chin, D. H. Wang and O. O. Park, *Macromol. Rapid Commun.*, 2010, **31**, 2095–2108.
62 E. L. Ratcliff, B. Zacher and N. R. Armstrong, *J. Phys. Chem. Lett.*, 2011, **2**, 1337–1350.
63 C.-P. Chen, C. Luo, C. Ting and S.-C. Chuang, *Chem. Commun.*, 2011, **47**, 1845–1847.
64 M. Mas-Torrent and C. Rovira, *Chem. Soc. Rev.*, 2008, **37**, 827–838.
65 I. McCulloch, M. Heeney, C. Bailey, K. Genevicius, I. MacDonald, M. Shkunov, D. Sparrowe, S. Tierney, R. Wagner, W. Zhang, M. L. Chabinyc, R. J. Kline, M. D. McGehee and M. F. Toney, *Nat. Mater.*, 2006, **5**, 328–333.

 This journal is © The Royal Society of Chemistry 2015